Optimal laser control of ultrafast photodissociation of I2 in water: Mixed quantum/classical molecular dynamics simulation

doi: 10.1063/1.1771640

Optimal laser control of ultrafast photodissociation of I_2^- in water: Mixed quantum/classical molecular dynamics simulation

Yoshikazu Nishiyama, Tsuyoshi Kato, Yukiyoshi Ohtsuki,[a] and Yuichi Fujimura
Department of Chemistry, Graduate School of Science, Tohoku University, Sendai 980-8578, Japan

(Received 12 May 2004; accepted 19 May 2004)

A linearized optimal control method in combination with mixed quantum/classical molecular dynamics simulation is used for numerically investigating the possibility of controlling photodissociation wave packets of I_2^- in water. Optimal pulses are designed using an ensemble of photodissociation samples, aiming at the creation of localized dissociation wave packets. Numerical results clearly show the effectiveness of the control although the control achievement is reduced with an increase in the internuclear distance associated with a target region. We introduce effective optimal pulses that are designed using a statistically averaged effective dissociation potential, and show that they semiquantitatively reproduce the control achievements calculated by using optimal pulses. The control mechanisms are interpreted from the time- and frequency-resolved spectra of the effective optimal pulses. © *2004 American Institute of Physics.* [DOI: 10.1063/1.1771640]

I. INTRODUCTION

In the last several years, we have witnessed significant advances toward achieving quantum control over a wide range of molecular dynamics using ultrafast laser pulses that are optimally designed by the so-called closed loop experiments.[1,2] A number of successful quantum control experiments have been reported, some of which deal with molecular dynamics in condensed phases.[3–9] They include the photochemistry of dyes[3] and coordination complexes,[4,6,9] pulse propagation in liquids,[5] vibrational dynamics in crystalline polymers,[7] and energy flow in biological systems.[8] Although those studies clearly show the basic principles of quantum control, it is still unclear how efficiently the dynamics in condensed phases can be coherently manipulated because quantum interferences are easily destroyed by dissipation processes. To answer this question, we conduct a case study of the manipulation of photodissociation of I_2^- in water by means of an optimal control method in combination with mixed quantum/classical molecular dynamics (MD) simulation.[10,11] As the strong solute-solvent interaction corresponds to the most unfavorable condition, we will show the limits of the quantum control in condensed phases.

Our theoretical analyses consist of two steps: the design of optimal pulses and the decoding of the designed pulses. Laser pulse design algorithms based on the optimal control theory are expressed in the form of inverse problems, which lead to coupled nonlinear pulse design equations with specified initial and final conditions.[12] Although efficient monotonically convergent algorithms within the density matrix formalism have been proposed, their iterative solution requires time-consuming computations.[13–17] This situation imposes restrictions on the theoretical treatment of condensed-phase dynamics,[18–23] that is, the whole system is divided into a (relevant) system and a heat bath, in which the bath degrees of freedom are explicitly or implicitly removed by appropriate assumptions. In addition, the system is often approximated by a prototype model, the time evolution of which is described by using the optical Bloch equation[13,17,18] and the master equation with/without memory effects.[15,19,21–23] The advantage of such modeling is that it facilitates understanding of the behavior of condensed-phase dynamics and the examination of the control mechanisms in detail, whereas the disadvantage is that we always reach qualitative conclusions.

By restricting ourselves to a weak field regime, we have a linearized pulse design equation expressed in terms of a molecular response function.[24–28] This approach has been extensively developed by Wilson and co-workers.[24–27] This simplification imposes less restrictions for describing molecular dynamics in condensed phases. In fact, various approximations, such as harmonic as well as anharmonic Brownian oscillators,[24,27] classical MD simulations,[25] and the time-dependent Hartree (TDH) approximation,[26] have been implemented to calculate the molecular response functions and thus the optimal pulse.

Of several available approaches, mixed quantum/classical MD simulation is considered to be a powerful tool for numerically investigating molecular response functions in condensed phases.[10,11,28] In this case, the system is treated quantum mechanically, whereas the heat bath is treated classical mechanically. The system (heat bath) acts on the heat bath (system) through the Hellman–Feynman force (mean field). Because of the flexibility in choosing the system size, the time evolution of the whole system can be calculated within reasonable computational time. According to this pulse design scheme, Guiang and Wyatt[28] studied the quantum control of I_2 wave packet localization in the electronically excited state in an Ar matrix within a low temperature range. The I_2/Ar system can be regarded as a prototype system with weak solute-solvent interactions, and therefore an ideal condensed-phase system for quantum control.[29,30]

In the present work, we deal with the quantum control of

[a]Author to whom correspondence should be addressed. Electronic-mail: ohtsuki@mcl.chem.tohoku.ac.jp

a I_2^-/H_2O system that is characterized by strong solute-solvent interactions. We construct an ensemble of photodissociation samples using classical MD simulations. An optimal pulse is designed so that it maximizes the statistical average of a specified target yield over the ensemble. We employ the linearized optimal control procedure in combination with mixed quantum/classical MD simulation in order to design an optimal pulse that generates a localized dissociation wave packet of I_2^- in the excited electronic state. The control mechanisms are interpreted by using a statistically averaged effective dissociation potential, which is introduced in Sec. IV.

From an experimental viewpoint, I_2^- (Br_2^-) has been regarded as a prototype molecule for exploring photodissociation dynamics in the presence of strong solute-solvent interactions since the pioneering work by Lineberger's group[31,32] who studied the dynamics using size-selected clusters.[31–33] In solutions, real-time measurements of the photodissociation and the subsequent caging dynamics of I_2^- were conducted by Barbara's group.[34–36] These observations[31–36] were consistently interpreted by MD simulations.[37–42] Because of available knowledge regarding the I_2^-/H_2O system, it may serve as an ideal tool for experimentally investigating the possibility of quantum control in condensed phases.

This paper is organized as follows: In Sec. II, the mixed quantum/classical equations of motion and the linearized pulse design equation are presented. After describing the numerical details (Sec. III), we discuss the numerical results in Sec. IV, and give a summary in Sec. V.

II. THEORY

The Hamiltonian of a whole system is divided into a (relevant) system Hamiltonian, H_S^0, a heat bath Hamiltonian, H_B^0, and the interaction between them, V_{SB}:

$$H_T = H_S^0 + V_S^t + H_B^0 + V_{SB}, \tag{1}$$

where V_S^t is the interaction between the relevant system and a laser field, $E(t)$. Here, the heat bath is assumed to be optically inactive. Considering a two-electronic-state system, we express H_S^0 as the sum of two vibronic Hamiltonians:

$$H_S^0 = |g\rangle H_g^0 \langle g| + |e\rangle H_e^0 \langle e|, \tag{2}$$

where H_g^0 (H_e^0) denotes the vibrational Hamiltonian in the ground (excited) state, $|g\rangle$ ($|e\rangle$). For the optical interaction, we assume the rotating-wave approximation within the semiclassical dipole interaction:

$$V_S^t = -\mu_+ \epsilon(t) - \mu_- \epsilon^*(t), \tag{3}$$

where $\mu_+ = (\mu_-)^\dagger$ is the dipole moment operator associated with absorption (emission) processes. In Eq. (3), we write the laser field in the form, $E(t) = \epsilon(t) + \epsilon^*(t)$ to extract the rotating parts from $E(t)$.

The time evolution of a whole system is described by a total density operator, $\rho_T(t)$, which obeys the quantum Liouville equation

$$i\hbar \frac{\partial}{\partial t} |\rho_T(t)\rangle\rangle = L_T |\rho_T(t)\rangle\rangle = (L_S^0 + K_S^t + L_B^0 + K_{SB}) |\rho_T(t)\rangle\rangle, \tag{4}$$

where the double-space (Liouville-space) notation is used.[43] The Liouvillians, $L_T = L_S^0 + K_S^t + L_B^0 + K_{SB}$, correspond to the commutators of the Hamiltonians in Eq. (1), i.e., $[H_T, \cdots] = [H_S^0 + V_S^t + H_B^0 + V_{SB}, \cdots]$. We apply the TDH approximation to the total density operator in order to factorize it in the product form:

$$|\rho_T(t)\rangle\rangle = |\rho(t)\rangle\rangle |\rho_B(t)\rangle\rangle, \tag{5}$$

where $|\rho(t)\rangle\rangle$ ($|\rho_B(t)\rangle\rangle$) is the system (heat bath) density operator. The system potential is modified by the mean-field interaction due to the instantaneous coupling with the heat bath,

$$\langle V_{SB}(t)\rangle_B = \mathrm{Tr}_B\{\rho_B(t) V_{SB}\}. \tag{6}$$

We have the equation of motion for the relevant system

$$i\hbar \frac{\partial}{\partial t} |\rho(t)\rangle\rangle = [L_S^0 + K_S^t + \langle K_{SB}(t)\rangle_B] |\rho(t)\rangle\rangle, \tag{7}$$

where $\langle K_{SB}(t)\rangle_B \leftrightarrow [\langle V_{SB}(t)\rangle_B, \cdots]$, with the initial condition of $|\rho(0)\rangle\rangle = |\rho_0\rangle\rangle$. For the density operator of the heat bath, we assume spatially localized distributions, and that the mean value of a function of the bath coordinates is equal to its value for the mean value of the coordinates. This assumption leads to

$$\mathrm{Tr}_B\{\rho_B(t) V_{SB}(\mathbf{r}, \mathbf{Q})\} \simeq V_{SB}(\mathbf{r}, \langle \mathbf{Q}(t)\rangle_B), \tag{8}$$

where $\mathbf{r}$ ($\mathbf{Q}$) denotes a set of the system (heat bath) coordinates.[44] If we rewrite $\langle \mathbf{Q}(t)\rangle_B$ as $\mathbf{Q}(t)$ for simplicity, the average values of the jth coordinate, $Q_j(t)$, and its conjugate momentum, $P_j(t)$, satisfy the canonical equations of classical mechanics with a classical Hamilton function, H_B^{cl},

$$\dot{Q}_j = \frac{\partial H_B^{cl}}{\partial P_j}, \tag{9a}$$

and

$$\dot{P}_j = -\frac{\partial H_B^{cl}}{\partial Q_j}. \tag{9b}$$

Here, the classical Hamilton function is defined by

$$H_B^{cl} = H_B^{cl}(\mathbf{Q}, \mathbf{P}) = H_B^0(\mathbf{Q}, \mathbf{P}) + \mathrm{Tr}_S\{\rho(t) V_{SB}(\mathbf{Q})\}, \tag{10}$$

where $\mathbf{Q}$ and $\mathbf{P}$ are regarded as classical variables. The last term in Eq. (10) gives the Hellmann-Feynman force, which describes the action from the quantum system to the classical heat bath.

An optimal pulse is designed so that it achieves the largest transition probability from an initial state to an objective state specified by a target operator W subject to minimum pulse fluence. The target operator is assumed to have a maximum expectation value when the system reaches the objective state. Then, the optimal pulse is defined by the electric field $\epsilon(t)$ that maximizes the following cost functional with a specified control time t_f:

$$J=\langle\langle W|\rho(t_f)\rangle\rangle-\lambda\int_0^{t_f}dt|\epsilon(t)|^2, \tag{11}$$

where a positive constant λ weighs the physical significance of the penalty due to pulse fluence. If we assume a weak laser field, the density operator in Eq. (11) can be approximated by the second-order perturbation solution with respect to the optical interaction, V_S^t. Under the constraint of the second-order perturbation solution, we apply calculus of variations to Eq. (11), and obtain the following linearized pulse design equation:[24]

$$\int_0^{t_f}d\tau M(t,\tau)\epsilon(\tau)=\lambda\epsilon(t), \tag{12}$$

where the molecular response function is given by

$$M(t,\tau)=\frac{1}{\hbar^2}\langle\langle W|G_{ee}(t_f,\tau)\hat{\mu}_+G_{ge}(\tau,t)\tilde{\mu}_+G_{gg}(t,0)|\rho_0\rangle\rangle \times\theta(\tau-t)+\frac{1}{\hbar^2}\langle\langle W|G_{ee}(t_f,t)\tilde{\mu}_+G_{eg}(t,\tau) \times\hat{\mu}_+G_{gg}(\tau,0)|\rho_0\rangle\rangle\theta(t-\tau). \tag{13}$$

Here the θ function is defined by $\theta(x)=1$ when $x>0$ and $\theta(x)=0$ when $x\leqslant 0$. The cap ($\hat{\mu}_+$) and tilde ($\tilde{\mu}_+$) space operators denote left-hand-acting and right-hand-acting operators, respectively. The double-space operators G_{gg}, $G_{ge}(G_{eg})$, and G_{ee}, describe the time evolution for $\rho_{gg}=\langle g|\rho|g\rangle$, $\rho_{ge}(\rho_{eg})$, and ρ_{ee}, respectively, in the absence of the system-laser interaction. The time orderings in these operators originate from the time-dependent mean fields.

When we consider the maximization of the target expectation value averaged over an ensemble constructed by MD simulations, we employ another objective functional expressed as

$$J=\frac{1}{N}\sum_{k=1}^{N}\langle\langle W|\rho^{(k)}(t_f)\rangle\rangle-\lambda\int_0^{t_f}dt|\epsilon(t)|^2, \tag{14}$$

where $|\rho^{(k)}(t)\rangle\rangle$ is the density operator of the kth sample, and N is the total number of samples included in the ensemble. Within a weak-field regime, we derive the same linearized pulse design equation as Eq. (12), in which, however, the molecular response function is replaced with the statistically averaged function:

$$M(t,\tau)=\frac{1}{N}\sum_{k=1}^{N}M^{(k)}(t,\tau). \tag{15}$$

In Sec. IV, we numerically design optimal pulses using this statistically averaged molecular response function.

The integral equation (eigenvalue equation), Eq. (12), has real eigenvalues, {λ}, which are guaranteed by the hermiticity of the integral kernel, $M(t,\tau)=M^*(\tau,t)$. The optimal pulse is given by the eigenvector associated with the largest eigenvalue, which leads to the largest expectation value of the target operator normalized by the pulse fluence:

$$\frac{1}{N}\sum_{k=1}^{N}\langle\langle W|\rho^{(k)}(t_f)\rangle\rangle=\lambda\int_0^{t_f}dt|\epsilon(t)|^2. \tag{16}$$

Equation (16) is proved in a straightforward manner. We multiply both sides of Eq. (12) by $\epsilon^*(t)$, and then integrate over $t\in[0,t_f]$. The resulting expression is rewritten using the expression of the target expectation value within the second-order perturbation approximation with respect to V_S^t. Utilizing the following equality, which is valid for an arbitrary function, $f(t,\tau)$,

$$\int_0^{t_f}dt\int_t^{t_f}d\tau f(t,\tau)=\int_0^{t_f}dt\int_0^{t}d\tau f(\tau,t), \tag{17}$$

we obtain Eq. (16).

Next, we will make some assumptions in calculating the time evolution of the system. Assuming stationary thermal fluctuations, we neglect the time orderings in the time-evolution operators so that they depend on only the time intervals. Because of the stochastic nature of the system-bath interaction, we further assume that the system is initially in thermal equilibrium. Thus, the ground state, time-evolution operator, G_{gg}, operates on $|\rho_0\rangle\rangle$ to give

$$G_{gg}(t,0)|\rho_0\rangle\rangle=|\rho_0\rangle\rangle, \tag{18}$$

where ρ_0 represents the Boltzmann distribution. After optical excitation, we solve the coupled equations, Eqs. (7) and (9), to determine the time evolution of the system in the electronic excited state.

Under these approximations, the molecular response function of the kth sample is rewritten as

$$M^{(k)}(t,\tau)=\frac{1}{\hbar^2}\mathrm{Tr}\{WU_e^{(k)}(t_f-\tau)\mu_+U_g^{(k)}(\tau-t) \times\rho_0\mu_-U_e^{(k)\dagger}(t_f-t)\}. \tag{19}$$

Here, the operators, $U_g^{(k)}$ and $U_e^{(k)}$, describe the time evolution of the kth system in the electronic ground and excited states, respectively. Note that the approximated integral kernel in Eq. (19), is also Hermitian, $M^{(k)}(t,\tau)=M^{(k)*}(\tau,t)$.

III. COMPUTATIONAL METHODS

In this section, we introduce the potential parameters (Sec. III A), explain the numerical details of our MD simulations (Sec. III B), specify control targets (Sec. III C), and summarize the numerical procedure for calculating optimal pulses (Sec. III D).

A. Model potentials

In our MD calculations, we employ a cubic main cell that contains one I_2^-, a counter cation, Na^+, and 254 water molecules modeled by SPC/E.[45] (The density of water is 1.023 g/cm^3.) The photodissociation dynamics of I_2^- is approximated by a one-dimensional, two-electronic-state model. The electronic ground state potential of I_2^- is modeled by a Morse oscillator, the potential parameters of which are taken from Ref. 46. The dissociation energy, the equilibrium distance and the range parameter are given by $D_e=1.1$ eV, $r_e=3.23$ Å, and $\beta=1.16$ Å, respectively. The harmonic frequency of this potential is in good agreement with the experimentally observed value of ~115 cm^{-1} of I_2^- in water.[47] The excited-state potential, on the other hand, is modeled by

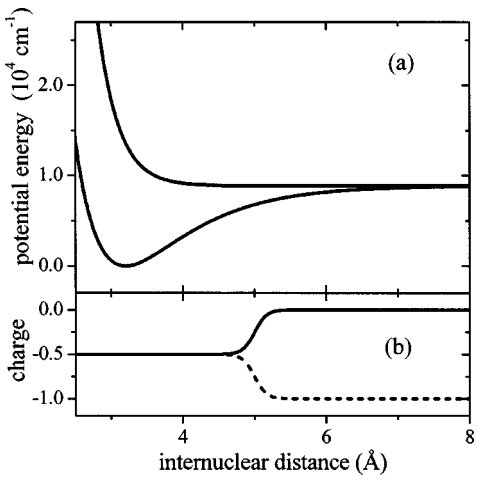

FIG. 1. (a) One-dimensional, two-electronic-state model for I_2^-, and (b) a charge switching function [Eq. (20)].

an exponential function, $V_0 \exp[-\beta(r-r_e)]$ with $V_0 = 0.59$ eV, $r_e = 3.23$ Å, and $\beta = 3.50$ Å.[48,49] The excess dissociation energy estimated at ~0.59 eV corresponds to a dissociation time of 170 fs if we neglect solvent effects.[50] Although this is rather a simple model, it is known to semiquantitatively reproduce the transient absorption spectra observed by Kliner *et al.*[35]

As I_2^- dissociates, the excess electron initially delocalized over the anion becomes localized on one of the iodine atoms. We describe such a charge separation process with a switching function introduced by Perena and Amar,[37,51] which is given by

$$q_{1,2}(r) = -0.5e(1 \pm \tfrac{1}{2}\{1 + \tanh[\eta(r-\varsigma)]\}), \tag{20}$$

where ς specifies the distance at which the separation occurs, and η denotes the width of the interval over which the separation occurs. According to their criteria,[37] we choose $\varsigma = 5.0$ Å, which corresponds to the distance at which the bound energy of the ground-state iodine is reduced to 25% compared to that at the equilibrium position, and $\eta = 6.0$ Å^{-1}. We neglect any delocalization of ionic charge from the anion onto the surrounding water. The model potential and the charge switching function are illustrated in Fig. 1.

The water-solute intermolecular potentials are approximated by a sum of Lennard-Jones and Coulomb potentials,

$$V(r_{ij}) = 4\epsilon_{ij}\left[\left(\frac{\sigma_{ij}}{r_{ij}}\right)^{12} - \left(\frac{\sigma_{ij}}{r_{ij}}\right)^{6}\right] + \frac{q_i q_j}{r_{ij}} \tag{21}$$

with the standard combining rules

$$\sigma_{ij} = \tfrac{1}{2}(\sigma_i + \sigma_j),$$

and

$$\epsilon_{ij} = \sqrt{\epsilon_i \epsilon_j}. \tag{22}$$

As regards the Lennard-Jones parameters of the partially charged iodine, I^q $(-1 \leqslant q \leqslant 0)$, σ is chosen as $\sigma(q) = 4.987 - 0.178q$ (Å), whereas ϵ has a charge-independent value of 0.100 kcal/mol, which reproduce the parameters given in Ref. 52 in the two limiting cases, $q = 0$ and $q = -1$. We further assume that the parameters do not depend on the electronic state of I_2^-. For the water-Na^+ potential, the parameters are taken from Ref. 53. The Ewald method is used for calculating the Coulomb interaction, in which the cutoff length, the damping parameter and the maximum momentum are set at 15.0 Å, 0.32 Å^{-1}, and $10 \times 2\pi$/(cell-length), respectively.

B. Numerical simulations

An equilibrium molecular configuration is constructed by the 15 ps classical NVT calculations using the Nosé thermostat at $T = 300$ K. The 5 ps NVE run follows to generate a microcanonical ensemble. The equations of motion are numerically solved by the predictor-corrector method with a 0.1 fs time grid.[54] In these calculations, I_2^- is assumed to be in the ground electronic state.

The mixed quantum/classical calculation starts with the initial configuration prepared by the classical simulation. The classical internal motion of I_2^- is replaced with the thermal distribution of the Franck-Condon wave packet, which is uniformly discretized by 2048 grid points over the range of [1.7 Å, 17.0 Å]. Its time evolution is solved by the split-operator+fast Fourier transform scheme with a time grid of 0.02 fs. The mean-field potential and the Helmann–Feynman force are calculated every 0.1 fs. In our simulations, the electronic transitions of I_2^- are induced by the optical interaction but not by the mean-field interaction. Finally, to see the replacement effects on the following time evolution of the wave packet, we carry out an extra NVE run using the mixed quantum/classical calculation for several time intervals, and find that the difference is so small that no distinction in the shape of the wave packets can be recognized (not shown here).

C. Control targets

We specify the control targets after introducing the microscopic picture of the photodissociation dynamics of diiodine anion in a polar solvent. The photodissociation is initiated by optical excitation to an antibonding state. According to Parson *et al.*[41], immediately after the excitation, the excess charge of the ion moves to the less solvated atom. This anomalous charge flow leads to strong Coulomb interactions that pull the solute together and prevent it from dissociating. Thus, the dissociation only occurs after a nonadiabatic transition to an electronic state associated with "normal" charge flow. This explains the low quantum dissociation yield, e.g., ~0.12, in the case of an aqueous solution.[36,55]

The natural choice of the control objective may be to increase the dissociation yield; however, it is not a trivial target. As mentioned above, the dissociation is induced by a nonadiabatic transition to form solvated iodine ions, which can be attributed to charge transfer and/or solvent transfer.[56] Although solvent reorganization plays an important role in both cases, the optimal pulse cannot directly control solvent motion because we assume an optically inactive solvent. Besides, the numerical description of a nonadiabatic transition requires more electronic states, resulting in time-consuming computations beyond our computational resources. In the present work, we thus restrict ourselves to the control of a

dissociation wave packet using the two-electronic-state model [Fig. 1(a)]. Nonadiabatic transitions are effectively included in simulation using the charge switching function [Fig. 1(b)] without explicitly evaluating them.

Because of the low quantum yield of photodissociation, we first collect the dissociation samples by using classical MD calculations, which are described in Sec. III D. We design optimal pulses with the aim of maximizing the statistically averaged population in the region **R** at a specified internuclear distance at a control time. This control objective is denoted by the target operator

$$W=\int_{\mathbf{R}}|r\rangle dr\langle r|, \tag{23}$$

with r being the coordinate of the internuclear distance of I_2^-. As the target operator is represented by an integral (sum) of projectors, the control yield is not limited by the statistical distribution of the dissociation samples.[22,57]

D. Summary of numerical procedure for calculating optimal pulses

Step 1. Collecting dissociation samples: Starting with the initial molecular configuration prepared in Sec. III B, we perform the classical MD simulation to collect dissociation samples according to the scheme described below. At every 1 ps, we check if I_2^- dissociates in the given configuration, that is, we calculate the trajectories using the excited-state potential of I_2^- instead of the ground-state potential. If the internuclear distance of I_2^- exceeds 6.0 Å within 300 fs, it is regarded as a dissociation sample. Once we find a dissociation sample, we stop collecting dissociation samples for 5 ps in order to remove possible statistical correlation between adjacent dissociation samples. According to this scheme, we collect 30 dissociation samples. Based on the above criterion, we have a dissociation yield of 8.8%, in good agreement with the experimentally measured value of ~12%. Finally, we randomly choose 20 samples from the 30 dissociation samples to reduce computational burden in the following steps.

Step 2. Calculating statistically averaged molecular response function, Eq. (15): As shown in Eq. (19), the molecular response function is expressed in terms of the time evolution of the thermal distribution of the Franck–Condon wave packets. The time-dependent wave functions are obtained by numerically integrating the mixed quantum/classical equations. All the data of the time-dependent mean fields are stored in memory, which are required for evaluating control achievement in the next step. To calculate Eq. (15), we take the statistical average of each molecular response function over the thermal distribution as well as the dissociation samples.

Step 3. Calculating optimal pulse and control achievement: The diagonalization of the statistically averaged molecular response function gives the optimal pulse, which is the eigenstate associated with the largest eigenvalue. The calculated optimal pulse is used for evaluating control achievement defined by

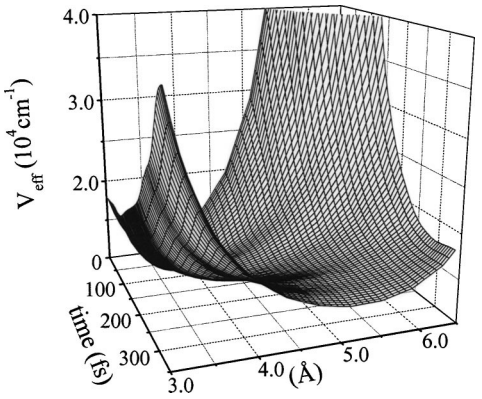

FIG. 2. Effective potential defined by Eq. (25).

$$Y(t)=\sqrt{\frac{\Sigma_{k=1}^{20}\langle W(t)\rangle^{(k)}}{\Sigma_{k=1}^{20}P_e^{(k)}(t)}}, \tag{24}$$

where $\langle W(t)\rangle^{(k)}$ and $P_e^{(k)}(t)$ are, respectively, the target expectation value and the excited-state population of the kth sample. We calculate $\langle W(t)\rangle^{(k)}$ and $P_e^{(k)}(t)$ using the optimal pulse and the mean fields of the kth sample (stored in memory). We perform this for each sample and substitute all the results into Eq. (24) to evaluate the control achievement. The definition of the control achievement in Eq. (24) can be rationalized by the fact that we always observe a statistically averaged quantity. When all samples are equivalent, the control achievement in Eq. (24) is reduced to that defined in previous papers.[24–26]

IV. NUMERICAL RESULTS AND DISCUSSION

Before discussing the numerical results, we introduce a statistically averaged dissociation potential of I_2^-, which is simply called an effective potential in this paper. The effective potential is defined by

$$V_{\text{eff}}(r,t)=V_0\exp[-\beta(r-r_e)]+\frac{1}{N}\sum_{k=1}^{N}V_{SB}(r,\langle\mathbf{Q}(t)\rangle^{(k)}), \tag{25}$$

where $V_0\exp[-\beta(r-r_e)]$ is the excited-state potential of I_2^- and $V_{SB}(r,\langle\mathbf{Q}(t)\rangle^{(k)})$ is the mean-field potential of the kth sample. Figure 2 shows the effective potential as a function of time and internuclear separation, which is characterized by a huge barrier around the initial time and a flat structure after ~250 fs. This is because after ~250 fs, all the samples contributing to the dissociation must have repulsive potentials, whereas around the initial time, no restrictions are imposed on the potential shapes. In fact, some of the samples initially have bound potentials, and introduce the barrier into the effective potential. The potential barrier gradually disappears due to solvent reorganization that occurs on the same time scale as the photo-dissociation of I_2^- at 300 K.

The effective potential is expected to extract the characteristic properties of the ensemble. We also design an optimal pulse using the effective potential, and refer to it as the effective optimal pulse in this paper. We substitute the effective optimal pulse into the equations of motion to calculate the

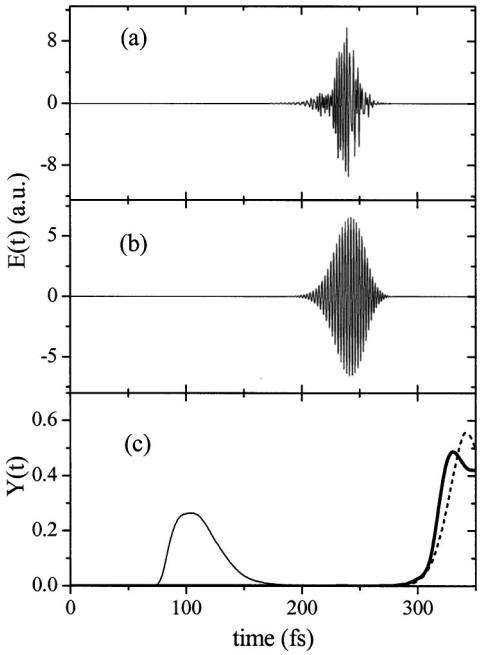

FIG. 3. For the target region, $\mathbf{R}\in[4.0, 4.1\ \text{Å}]$, (a) the optimal pulse, (b) the effective optimal pulse, and (c) the control achievements calculated by the optimal pulse (bold-solid line), the effective optimal pulse (bold-dashed line) and the Franck–Condon wave packet (thin solid line). Arbitrary units (a.u.) are used for the electric field amplitudes.

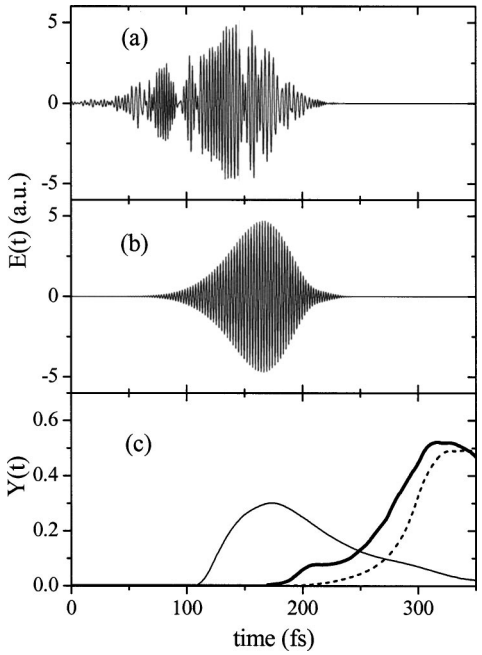

FIG. 4. For the target region, $\mathbf{R}\in[4.5, 4.7\ \text{Å}]$, (a) the optimal pulse, (b) the effective optimal pulse, and (c) the control achievements calculated by the optimal pulse (bold-solid line), the effective optimal pulse (bold-dashed line) and the Franck–Condon wave packet (thin solid line). Arbitrary units (a.u.) are used for the electric field amplitudes.

target expectation value and the excited-state population of each sample. The insertion of these values in Eq. (24) yields the statistically averaged control achievement realized by the effective optimal pulse.

Optimal pulses are designed with the aim of generating a localized wave packet at $\mathbf{R}\in[4.0, 4.1\ \text{Å}]$, $\mathbf{R}\in[4.5, 4.7\ \text{Å}]$, and $\mathbf{R}\in[5.0, 5.2\ \text{Å}]$, which are shown in Figs. 3, 4, and 5, respectively. The first target region has a width of 0.1 Å, whereas the other two regions have a width of 0.2 Å as the control of wave packet motion at a longer internuclear distance becomes more difficult. The target region of $\mathbf{R}\in[5.0, 5.2\ \text{Å}]$ corresponds to the internuclear distance immediately after the charge localization occurs. All the target regions are within the first solvation shell. (The possibility of controlling wave packet dynamics beyond the first solvation shell is shown in Fig. 7.)

Figures 3(a) and 3(b) show the optimal pulse and the effective optimal pulse, respectively. Arbitrary units (a.u.) are used for the electric field amplitudes as we assume the weak-field regime. In Fig. 3(c) the control achievement calculated by using the (effective) optimal pulse is represented by a bold-solid (bold-dashed) line. For reference, the thin solid line shows the control achievement associated with the Franck–Condon wave packet, in which we do not take the statistical average of the time evolution of the Franck–Condon wave packet over the thermal distribution and the samples. In Figs. 3(c), 4(c), and 5(c), the timing at which the control achievement becomes a maximum is slightly different from the control time, $t_f=350\,\text{fs}$. This is because the number of dissociation samples is not sufficiently large for realizing a stationary heat bath, which is assumed in our calculations (Sec. II). Another reason, which may be less important than the above, is that the target in the cost functional [Eq. (14)] is to maximize the target expectation value, not the control achievement.

Comparing the results in Figs. 3–5, we summarize the numerical observations as follows:

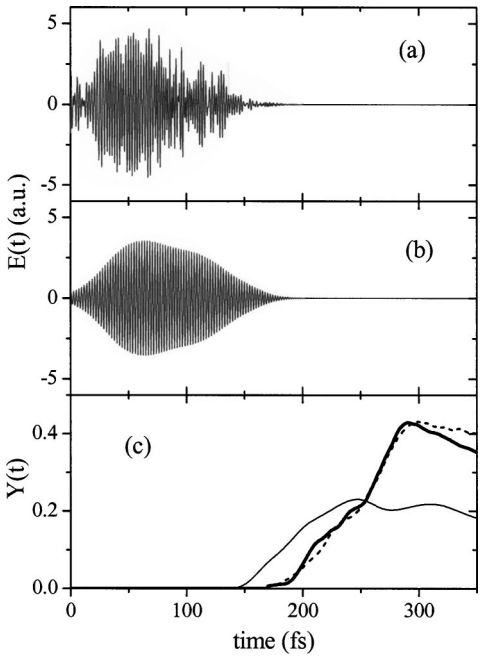

FIG. 5. For the target region, $\mathbf{R}\in[5.0, 5.2\ \text{Å}]$, (a) the optimal pulse, (b) the effective optimal pulse, and (c) the control achievements calculated by the optimal pulse (bold-solid line), the effective optimal pulse (bold-dashed line) and the Franck–Condon wave packet (thin solid line). Arbitrary units (a.u.) are used for the electric field amplitudes.

(A) Comparing the peak values of the control achievements, the designed optimal pulses always lead to nearly two times greater control achievements than those obtained by the Franck–Condon wave packet [Figs. 3(c), 4(c), and 5(c)].

(B) The optimal pulse has a larger temporal width for the target region at a longer internuclear distance [Figs. 3(a), 4(a), and 5(a)].

(C) The effective optimal pulses have much simpler structures than the corresponding optimal pulses [Figs. 3(b), 4(b), and 5(b)]; however, the effective optimal pulses lead to almost the same control achievements as those calculated by the optimal pulses [Figs. 3(c), 4(c), and 5(c)].

Result (A) clearly shows that the optimal pulses can manipulate wave packet dynamics by means of coherent control. They generate a localized dissociation wave packet of I_2^-, with high probability even in the presence of strong solute-solvent interactions as well as statistical distributions. As the specified internuclear distance becomes longer, the control achievement is rapidly reduced due to the solute-solvent interactions. However, the control effects may be sufficiently large for us to experimentally observe some degree of wave packet localization. As the present case study deals with one of the most unfavorable systems for quantum control because of the strong solute-solvent coupling, result (A) suggests that a wide range of condensed-phase dynamics can be coherently controlled to achieve specified targets.

We can explain observation (B) in terms of the statistical distribution of the velocities of the wave packets, which is due to the inhomogeneous environment induced by the heat bath. Because an excited wave packet has nearly zero velocity immediately after optical excitation, the distribution width increases as the time required to reach a target region increases. Roughly speaking, wave packets with low velocities must be excited earlier than those with high velocities in order for all of them to meet together at a target region at a control time. Thus a temporally broader optimal pulse is needed to localize the ensemble of the wave packets at a longer internuclear distance.

Concerning observation (C), we first point out that the modulated structures in optimal pulses are largely attributed to the statistical distribution of the dissociation samples. If the optimal pulse is designed using one sample and not the ensemble, we virtually see no modulation in the calculated pulse (not shown here). The overall structure of the optimal pulse is determined by ''typical'' samples included in the ensemble. In this sense, the effective optimal pulse is predicted to be a good approximation to the optimal pulse as long as the effective potential can be regarded as a representative of the sample potentials. This prediction is supported by the numerical results in which the effective optimal pulses semi-quantitatively reproduce the control achievements calculated by using the optimal pulses. In Fig. 4(c), the control achievement calculated by using the effective optimal pulse appears with a time lag that is explained by the slight temporal peak shifts between the pulses in Figs. 4(a) and 4(b). In the following, we examine the control mechanisms using the effective optimal pulses.

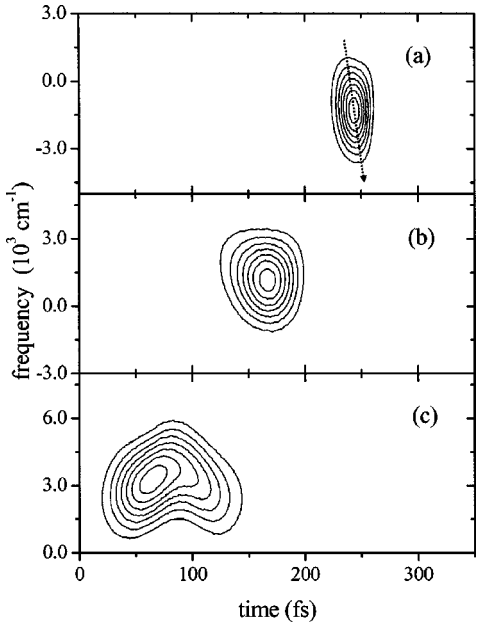

FIG. 6. (a) Time- and frequency-resolved spectrum of the effective optimal pulse in Fig. 3(b), (b) that in Fig. 4(b), and (c) that in Fig. 5(b). For convenience, the zero frequencies are chosen such that they correspond to the vertical transition energies at the equilibrium internuclear distance, $V_{\mathrm{eff}}(r_e,t)$.

The time- and frequency-resolved spectrum, $S(\omega,t)$, of the control pulse, $\epsilon(t)$, is calculated by

$$S(\omega,t)=\left|\int_{t-\tau_w/2}^{t+\tau_w/2} d\tau H(t-\tau,\tau_w)\,\epsilon(\tau)e^{i\omega\tau}\right|^2. \tag{26}$$

Here, the Blackman window function, $H(\tau,\tau_w)$, is defined by

$$H(\tau,\tau_w)=0.42+0.50\cos\left(\frac{2\pi}{\tau_w}\tau\right)+0.08\cos\left(\frac{4\pi}{\tau_w}\tau\right), \tag{27}$$

where the time resolution specified by the parameter, τ_w, is set at 10 fs. In Fig. 6, the calculated time- and frequency-resolved spectra of the effective optimal pulses in Figs. 3(b), 4(b), and 5(b), are, respectively, shown from top to bottom. For convenience, the frequencies are measured from the vertical transition energies at the equilibrium internuclear distance, i.e., we set $V_{\mathrm{eff}}(r_e,t)=0$. As the internuclear distance of the target is increased, the central frequency of the pulse is shifted to a higher frequency. This is because the wave packet must have extra energy to complement the energy dissipated by the heat bath during the propagation to a target. In addition, the wave packet with larger kinetic energy takes less time to reach the target and thus has less chances of interacting with the heat bath, resulting in a higher control yield.

We also see that the time- and frequency-resolved spectra have characteristic chirped structures. For example, in the case of $\mathbf{R}\in[4.0, 4.1\ \text{Å}]$, the effective optimal pulse shows slight negative chirping [Fig. 6(a)]. Because this target is located far from the first solvation shell, the solute-solvent interactions may play a minor role in the control. In such a system, a positively chirped pulse is often said to efficiently

create a spatially localized wave packet on a repulsive potential.[58] In our case, on the other hand, the target is localized very close to the Franck–Condon region, and also the curvature of the repulsive potential is smaller than those of the molecules studied so far. Because of the small curvature of the repulsive potential, small shifts in frequency correspond to large changes in the internuclear distance at which resonant vertical transitions occur. Under these conditions, in order to create a localized wave packet, we must first create the wave packet components initially at a small internuclear distance and then create those initially at a large internuclear distance. here, we call the former (latter) components small-distance (large-distance) components for simplicity. If both components are generated simultaneously, there is no chance for the small-distance components to catch up with the large-distance components because the target region is so close to the Franck–Condon region. Assuming resonant transitions, the small-distance components are generated by the high-frequency parts of the pulse, whereas the large-distance components are generated by the low-frequency parts of the pulse, resulting in the negatively chirped structure of the effective optimal pulse. Note that often times we numerically observe a Franck–Condon packet propagating on a repulsive potential being spatially squeezed at first and then becoming broad (not shown here). This may also support the above-mentioned control mechanisms.

For the target of $\mathbf{R}\in[4.5, 4.7\ \text{Å}]$, we do not see any particular chirping in the effective optimal pulse [Fig. 6(b)]. In this region, the statistical distribution as well as the dissipation processes can weaken the chirping effects on the control.

In Fig. 6(c), the effective optimal pulse associated with the target, $\mathbf{R}\in[5.0, 5.2\ \text{Å}]$, has an up-down chirped structure in the time- and frequency-resolved spectrum. Because of the low control achievement, it is difficult to say if this characteristic chirped structure of the effective optimal pulse is essential for the control.

To get a rough idea of the control mechanisms in the case of the $\mathbf{R}\in[5.0, 5.2\ \text{Å}]$ target, we calculate the time evolution of the dissociation wave packet generated by the effective optimal pulse. In this calculation, the system is assumed to be represented by a wave function under the influence of the time-dependent effective potential [Eq. (25)], that is, we do not take a statistical average. Figure 7 shows the calculated wave packet indicating that the first-half and the second half of the effective optimal pulse create the two separate wave packet components that meet at the target region at the control time. Note that the interference patterns shown in Fig. 7 have no physical importance because we ignore the statistical distribution in this analysis.

Finally, we briefly discuss the possibility of controlling wave packet dynamics outside the first solvation shell. In Fig. 7, we do not see any wave packet components that directly dissociate without being caught by the solvent cage. Remembering our method to collect ''dissociation'' samples, all the corresponding classical trajectories exceed 6.0 Å within 300 fs. Thus, the quantum nature of the dissociation makes it difficult for I_2^- to form independent fragment atoms outside the first solvation shell. This suggests that the photo-

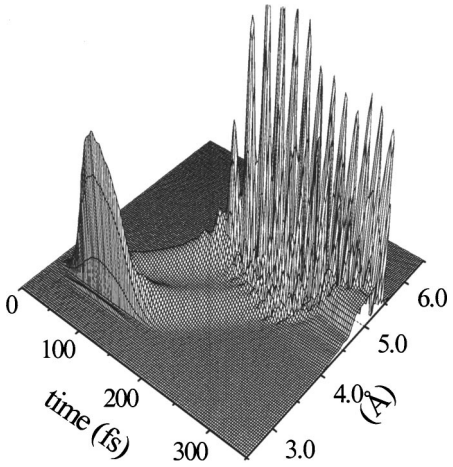

FIG. 7. Time evolution of the wave packet calculated using the effective optimal pulse in Fig. 5(b), in which we do not take a statistical average over the ensemble.

dissociation wave packet is initially trapped within the first solvation shell, which is destroyed by dissipation, and then the fragment atoms escape from this cage. The cage escape occurs on a much longer time scale than what we are currently concerned with. Recently, Apkarian and co-workers reported that the photoexcited I_2 in an Ar matrix with an excess energy of 4 eV can break the Ar cage with 50% probability.[30] This indicates that it is possible for a system with weak solute-solvent interactions to coherently control the dynamics of a dissociation wave packet outside a solvation shell. On the other hand, it is a real challenge to coherently control the wave packet outside the first solvation shell for the I_2^-/H_2O system because of the strong solute-solvent interactions.

V. SUMMARY

We have investigated the possibility of controlling the photo-dissociation dynamics of I_2^- in water using a linearized optimal control method. Mixed quantum/classical MD simulations were used to describe the time evolution of the whole system, in which the quantum system (solute) was coupled with the classical heat bath (solvent) through the Hellman–Feynman forces and the mean-field potentials. Optimal laser pulses were designed to maximize a statistically averaged target expectation value subject to minimum pulse fluence, using an ensemble of dissociation samples that were collected by classical MD simulations.

We numerically designed optimal pulses with the aim of creating a localized wave packet at three regions specified by different internuclear distances. The optimal pulses always led to approximately two times better achievements than those given by the thermal distribution of the Franck–Condon wave packets (the δ-function excitation). As the target internuclear distance was increased, the control achievements were decreased rapidly; however, there remained the coherent control effects that were experimentally observable.

We introduced an effective optimal pulse that was designed using the statistically averaged dissociation potential, called an effective potential here (Fig. 2). We found that the

effective optimal pulses semiquantitatively reproduced the control achievements calculated by the optimal pulses although the effective optimal pulses had much simpler structures than the optimal pulses. We examined the control mechanisms using the time- and frequency-resolved spectra of the effective optimal pulses. Because of the dissipation, we saw a high-energy shift in the central frequency of the pulse as the target internuclear distance was increased. When the target region was located at a small internuclear distance, the effective optimal pulse had a slightly negative chirped structure. From the time evolution of the wave packet, there was no wave packet component that broke and went outside the first solvation shell. It is necessary to develop new scenarios in order to coherently control wave packet dynamics outside the solvation shell for systems with strong solute-solvent interactions, such as the I_2^-/H_2O system.

ACKNOWLEDGMENTS

We are grateful to Professor T. Nakajima and Professor Y. Tanimura for helpful suggestions. We also acknowledge support from Grant-in-Aid for Scientific Research on Priority Areas ''Control of Molecules in Intense Laser Fields'' from the Ministry of Education, Culture, Sports, Science, and Technology (MEXT) of the Japanese Government.

[1] H. Rabitz, R. de Vivie-Riedle, M. Motzkus, and K. Kompa, Science **288**, 824 (2000).
[2] R. S. Judson and H. Rabitz, Phys. Rev. Lett. **68**, 1500 (1992).
[3] C. J. Bardeen, V. V. Yakovlev, K. R. Wilson, S. D. Carpenter, P. M. Weber, and W. S. Warren, Chem. Phys. Lett. **280**, 151 (1997).
[4] A. Assion, T. Baumert, M. Bergt, T. Brixner, B. Kiefer, V. Seyfried, M. Strehle, and G. Gerber, Science **282**, 919 (1998).
[5] T. C. Weinacht, J. L. White, and P. H. Bucksbaum, J. Phys. Chem. A **103**, 10166 (1999).
[6] T. Brixner, B. Kiefer, and G. Gerber, Chem. Phys. **267**, 241 (2001).
[7] D. Zeidler, S. Frey, W. Wohlleben, M. Motzkus, F. Busch, T. Chen, W. Kiefer, and A. Materny, J. Chem. Phys. **116**, 5231 (2002).
[8] J. L. Herek, W. Wohlleben, R. J. Cogdell, D. Zeidler, and M. Motzkus, Nature (London) **417**, 533 (2002).
[9] T. Brixner, N. H. Damrauer, B. Kiefer, and G. Gerber, J. Chem. Phys. **118**, 3692 (2003).
[10] *Classical and Quantum Dynamics in Condensed Phase Simulations*, edited by B. J. Berne, G. Ciccotti, and D. F. Coker (World Scientific, Singapore, 1998).
[11] T. Terashima, M. Shiga, and S. Okazaki, J. Chem. Phys. **114**, 5663 (2001).
[12] Y. Ohtsuki, K. Nakagami, and Y. Fujimura, Adv. Multi-photon Proc. Spectrosc. **13**, 3 (2000), and references therein.
[13] Y. Ohtsuki, W. Zhu, and H. Rabitz, J. Chem. Phys. **110**, 9825 (1999).
[14] Y. Ohtsuki, K. Nakagami, Y. Fujimura, W. Zhu, and H. Rabitz, J. Chem. Phys. **114**, 8867 (2001).
[15] Y. Ohtsuki, J. Chem. Phys. **119**, 661 (2003).
[16] Y. Ohtsuki and H. Rabitz, CRM Proc. Lect. Notes **33**, 163 (2003).
[17] Y. Ohtsuki, G. Turinici, and H. Rabitz, J. Chem. Phys. **120**, 5509 (2004).
[18] P. Gross, D. Neuhauser, and H. Rabitz, J. Chem. Phys. **94**, 1158 (1991).
[19] A. Bartana, R. Kosloff, and D. J. Tannor, J. Chem. Phys. **106**, 1435 (1997).
[20] P. Gross and S. D. Schwartz, J. Chem. Phys. **109**, 4843 (1998).
[21] K. Nakagami, Y. Ohtsuki, and Y. Fujimura, Chem. Phys. Lett. **360**, 91 (2002).
[22] Y. Ohtsuki, K. Nakagami, W. Zhu, and H. Rabitz, Chem. Phys. **287**, 197 (2003).
[23] R. Xu, Y.-J. Yan, Y. Ohtsuki, Y. Fujimura, and H. Rabitz, J. Chem. Phys. **120**, 6600 (2004).
[24] Y.-J. Yan, R. E. Gillilan, R. M. Whitenell, K. R. Wilson, and S. Mukamel, J. Phys. Chem. **97**, 2320 (1993).
[25] J. Che, M. Messina, K. R. Wilson, V. A. Apkarian, Z. Li, C. C. Martens, R. Zadoyan, and Y.-J. Yan, J. Phys. Chem. **100**, 7873 (1996).
[26] M. Messina, K. R. Wilson, and J. L. Krause, J. Chem. Phys. **104**, 173 (1996).
[27] J. Cao, M. Messina, and K. R. Wilson, J. Chem. Phys. **106**, 5239 (1997).
[28] C. S. Guiang and R. E. Wyatt, J. Chem. Phys. **112**, 3580 (2000).
[29] J. C. Bardeen, J. Che, K. R. Wilson *et al.*, J. Chem. Phys. **106**, 8486 (1997).
[30] Z. Bihary, R. Zadoyan, M. Karavitis, and V. A. Apkarian, J. Chem. Phys. **120**, 7576 (2004), and references therein.
[31] M. L. Alexander, N. E. Levinger, M. A. Johnson, D. Ray, and W. C. Lineberger, J. Chem. Phys. **88**, 6200 (1988).
[32] D. Ray, N. E. Levinger, J. M. Papanikolas, and W. C. Lineberger, J. Chem. Phys. **91**, 6533 (1989).
[33] B. J. Greenblatt, M. T. Zanni, and D. Neumark, J. Chem. Phys. **112**, 601 (2000).
[34] A. E. Johnson, N. E. Levinger, and P. F. Barbara, J. Phys. Chem. **96**, 7841 (1992).
[35] D. A. Kliner, J. C. Alfano, and P. F. Barbara, J. Chem. Phys. **98**, 5375 (1993).
[36] P. K. Walhout, J. C. Alfano, K. A. M. Thakur, and P. F. Barbara, J. Phys. Chem. **99**, 7568 (1995).
[37] L. Perena and F. G. Amar, J. Chem. Phys. **90**, 7354 (1989).
[38] I. Benjamin and R. M. Whitnell, Chem. Phys. Lett. **204**, 45 (1993).
[39] J. M. Papanikolas, P. E. Maslen, and R. Parson, J. Chem. Phys. **102**, 2452 (1995).
[40] C. J. Margulis and D. F. Coker, J. Chem. Phys. **110**, 5677 (1999).
[41] R. Parson, J. Faeder, and N. Delaney, J. Phys. Chem. A **104**, 9653 (2000), and references therein.
[42] E. Cho and S. Shin, J. Chem. Phys. **117**, 6047 (2002).
[43] K. Blum, *Density Matrix Theory and Application* (Plenum, New York, 1981).
[44] C. Cohen-Tannoudji, B. Diu, and F. Laloë, *Quantum Mechanics* (Hermann, Paris, 1977), Chap. III.
[45] H. J. C. Berendsen, J. R. Grigera, and T. P. Straatsma, J. Phys. Chem. **91**, 6269 (1987).
[46] E. C. M. Chen and W. E. Wentworth, J. Phys. Chem. **89**, 4099 (1985).
[47] G. N. R. Tripathi, R. H. Schuler, and R. W. Fessenden, Chem. Phys. Lett. **113**, 563 (1985).
[48] U. Banin, R. Kosloff, and S. Ruhman, Chem. Phys. **183**, 289 (1994).
[49] G. Ashkenazi, U. Banin, A. Bartana, R. Kosloff, and S. Ruhman, Adv. Chem. Phys. **100**, 229 (1997).
[50] R. Bersohn and A. H. Zewail, Ber. Bunsenges. Phys. Chem. **92**, 373 (1988).
[51] J. P. Bergsma, B. J. Gertner, K. R. Wilson, and J. T. Hynes, J. Chem. Phys. **86**, 1356 (1987).
[52] L. X. Dang and B. C. Garrett, J. Chem. Phys. **99**, 2972 (1993).
[53] S.-B. Zhu and G. W. Robinson, J. Chem. Phys. **97**, 4336 (1992).
[54] T. Kato and Y. Tanimura, J. Chem. Phys. **117**, 6221 (2002).
[55] V. Nagarajan and R. W. Fessenden, J. Phys. Chem. **89**, 2330 (1985).
[56] Within the mixed quantum/classical treatment, the nonadiabatic transition is caused by ''external fields'' associated with the classical solvent motion. Its matrix element thus has a quite similar expression to that induced by strong laser fields. J. Faeder, N. Delaney, P. E. Maslen, and R. Parson, Chem. Phys. **239**, 525 (1998); A. D. Bandrauk and H. Kono, Adv. Multi-photon Processes Spectrosc. **15**, 150 (2003).
[57] M. D. Girardeau, M. Ina, S. Schirmer, and T. Gulsrud, Phys. Rev. A **55**, R1565 (1997).
[58] J. L. Krause, R. M. Whitenell, K. R. Wilson, Y.-J. Yan, and S. Mukamel, J. Chem. Phys. **99**, 6562 (1993).